PAPER

Chemobrionic structures in tissue engineering: self-assembling calcium phosphate tubes as cellular scaffolds

Erik A. B. Hughes, [ID] *[a,b] Miruna Chipara, [ID] [a] Thomas J. Hall, [ID] [a] Richard L. Williams [ID] [a] and Liam M. Grover [ID] *[a]

A diverse range of complex patterns and mineralised hierarchical microstructures can be derived from chemobrionic systems, with formation driven by complex reaction–diffusion mechanisms far from thermodynamic equilibrium. In these experiments, self-assembling calcium phosphate tubes are generated using hydrogels made with 1 M calcium solutions layered with solutions of dibasic sodium phosphate over a range of concentrations between 0.2–1 M. Self-assembling structures prepared using 0.8 M dibasic sodium phosphate solutions were selected to assess cell–material interactions. Candidate chemobrionic scaffolds were characterised by micro-X-Ray fluorescence (μ-XRF) spectroscopy, Raman spectroscopy, powder X-ray diffraction (XRD), helium pycnometry and scanning electron microscopy (SEM). As prepared tubes were formed from non-stoichiometric hydroxyapatite (HA, $Ca_{10-x}(PO_4)_{6-x}(HPO_4)_x(OH)_{2-x}$ ($0 \leq x \leq 1$)), which was confirmed as calcium deficient hydroxyapatite (CDHA, $Ca_9(PO_4)_5HPO_4OH$). Thermal treatment of tubes in air at 650 °C for 4 h converted the structures to beta tricalcium phosphate (β-TCP, $β-Ca_3(PO_4)_2$). The potential of these scaffolds to support the attachment of bone marrow derived mesenchymal stem cells (BMSCs) was investigated for the first time, and we demonstrate cell attachment and elongation on the fabricated tubular structures.

Introduction

Chemobrionics describes the control and exploitation of the chemical and physical phenomena behind self-organisation reactions that result in the formation of abiotic macro-, micro- and nano-material architectures.[1] Nature gives rise to a diverse range of complex patterns, hierarchical structures and geological formations, many of which are derived from chemobrionic principles. Upon the ocean floor, hydrothermal vents emit hot mineral rich fluid that precipitates in contact with cool seawater to form chimney-like structures.[2] In the polar oceans, descending plumes of cold brine from sea ice freeze the water around them to form hollow tubes of ice known as brinicles.[3] Within limestone caves, the precipitation of mineral rich water dripping from the cave ceiling can result in the formation of stalactite and stalagmite structures.[4] Structures resembling such forms can be grown in a laboratory in several different ways. In the classical approach, a metal-salt seed is submerged in an anionic rich solution.[5–8] As the salt seed dissolves, a col-

loidal semi-permeable membrane forms around itself from the precipitation of cations and anions. Steep concentration and pH gradients can be promoted across the membrane, leading to a build-up in osmotic pressure. Eventually this pressure can rupture the membrane at several sites to release streams of cations into the solution. Precipitation around these buoyant streams gives rise to hollow tubular forms. These self-assembling structures, more commonly referred to as "Chemical gardens", were first described in 1646 by German-Dutch scientist Johann Glauber.[9] Not only are the observations of structures growing in these experiments of value as an educational tool,[10] they may also help mankind to understand extra-terrestrial mineral formations, such as those found on Saturn's moon, Enceladus.[11]

A resurgence in chemobiotic research interest has seen the advent of alternative and sophisticated methods of structural synthesis beyond a simple salt seed. For instance, precipitate self-assembly can also be made to occur at the interface between cation loaded hydrogels and anionic solutions.[12,13] These systems have also been adapted to accommodate the growth of mineral at non-planar surfaces, such as gel spheres encapsulated with reactant ions.[14,15] Alternatively, the controlled injection of a cationic solution into an anionic reservoir (and *vice versa*), can provide unique insights into growth

[a]*School of Chemical Engineering, University of Birmingham, B15 2TT, UK. E-mail: e.a.b.hughes@bham.ac.uk, l.m.grover@bham.ac.uk*
[b]*NIHR Surgical Reconstruction and Microbiology Research Centre, Queen Elizabeth Hospital, Birmingham, UK*

regimes during self-assembly and offer greater influence over precipitate composition.[16–19] Injection system set-ups can also be adapted to mimic the chemistry found in the early oceans of Earth in order to help understand the origins of life on our planet.[20–22]

Surprisingly, there is relatively little work that examines the use of such systems for biotechnological applications. Regenerative hard tissue scaffolds that offer through porosity and micro channels for cellular ingress are preferred to provide an environment for new tissue formation. The creation of such complex material geometries, whilst being both chemically and structurally similar to native bone, remains challenging.[23,24] However, we have recently shown that tubular calcium phosphate structures generated from a gel/solution interface closely resemble the structural motifs found in mineralised mammalian bones and teeth.[13] Furthermore, chemobrionic scaffolds have been shown to support biological components, only reinforcing the potential application of these intricate materials as regenerative cell supporting scaffolds.[14,25,26]

In this paper, the generation of calcium phosphate structures was systematically explored. Structures were characterised by micro-X-Ray fluorescence (μ-XRF) spectroscopy, Raman spectroscopy, powder X-ray diffraction (XRD), helium pycnometry and scanning electron microscopy (SEM), prior to seeding candidate structures with bone marrow derived mesenchymal stem cells (BMSCs). Biological interactions were investigated by means of fluorescence imaging and SEM to confirm cell viability and attachment.

Experimental

Fabrication of chemobrionic calcium phosphate structures

Calcium nitrate tetrahydrate ($Ca(NO_3)_2 \cdot 4H_2O$, 99%, ACS reagent) and agar ($((C_{12}H_{18}O_9)_n)$) were acquired from Sigma-Aldrich (Sigma-Aldrich, UK). Dibasic sodium phosphate heptahydrate ($Na_2HPO_4 \cdot 7H_2O$, 98+%, ACS reagent) was acquired from Acros Organics (Thermo Fisher Scientific, UK). The gel was produced by dissolving 1 M $Ca(NO_3)_2 \cdot 4H_2O$ and 5% w/v agar in 0.1 L distilled H_2O, stirring at 250 rpm and heated to 80–90 °C on an MR Hei-Standard magnetic stirrer hot plate (Heidolph, Germany). 5 mL of gel precursor solution was extruded into clear cylindrical containers using a 10 mL syringe and allowed to cool. Gels were stored at 4 °C overnight and heated to 60 °C for 15 min prior to usage to evaporate any condensation formed on the gel surface. The calcium concentration of the gel phase was kept at 1 M across all experiments. Phosphate solutions of varying concentration were prepared as specified.

Characterisation of candidate scaffolds

Micro- X-ray fluorescence (μ-XRF) spectra were acquired using an M4 Tornado instrument (Bruker, USA). Samples were exposed to a vacuum of 30 mbar within the instrument chamber with the X-ray tube operating at a voltage of 50 kV and an anode current of 300 mA. The presented data was an average of three accumulations collected over an acquisition time of

10 ms per measurement. Raman spectroscopy was performed using an inVia™ Raman microscope equipped with 532 nm laser and 2400 l mm⁻¹ grating (Renishaw Plc, UK). The presented scans were an average of three accumulations acquired at 100% power and 30 seconds exposure time. Powder X-ray diffraction (XRD) was performed using a D8 Advance diffractometer instrument equipped with a Cu X-ray source (1.5418 Å) and LYNXEYE (1D mode) detector (Bruker, USA). Diffraction patterns were acquired between 14–45° 2θ with a step size of 0.02° and step time of 0.3 seconds. Crystallisation was calculated in accordance with eqn (1). Scanning electron microscopy (SEM) was performed using a TM3030 table top scanning electron microscope (Hitachi, Japan). Samples were adhered onto double adhesive carbon discs attached to aluminium stubs. Samples were sputter coated before collecting secondary electron micrographs with the beam power at 10 kV. Structural density was obtained using an AccuPyc II 1340 helium pycnometer (Micrometrics, USA) over 5 cycles of 5 purges.

$$X_c \ (\%) = (I_c/(I_c + I_a)) \times 100 \tag{1}$$

where, X_c = percentage crystallinity, I_c = area of crystalline peaks and I_a = area of amorphous peaks ($I_c + I_a$ considers the total area under the diffraction pattern).

Stem cell culture and imaging

Sheep bone marrow derived mesenchymal stem cells (BMSCs) were isolated as described elsewhere.[27] BMSCs were cultured under standard culturing conditions in Dulbecco's modified Eagle's medium (DMEM) supplemented with 10% fetal bovine serum, 1% L-glutamine, 1% PenStrep and 1% nonessential amino acids (NEAA) at 37 °C and in 5% CO_2 atmosphere. Calcium phosphate tubes were sterilised with 70% ethanol followed by exposure to UV light for 30 min. The tubes were finally washed with culture media prior to adding samples to 12 well tissue culture suspension plates. BMSCs were seeded onto two types of tubes generated from the 0.8 M dibasic sodium phosphate system, as prepared tubes and thermally treated tubes, the latter of which were subjected to 650 °C in air for 4 h. All experiments were conducted at the same cell density of 2.5×10^5 cells per well. Cells were cultured for 48 h at 37 °C, 5% CO_2 conditions. The cells were then either stained with an R37609 ReadyProbes Cell Viability Blue/Green Imaging kit (Invitrogen, US) and imaged on an M5000 fluorescence microscope (EVOS, Thermo Fisher Scientific,), or fixed with 4% paraformaldehyde for further characterisation. The quantitative analysis of the viability assay was calculated using CellProfiler software (3.1.5) by identifying primary objects (nuclei) and measuring the total intensity from areas enclosed by the objects. A proportion of the fixed cells and tubes were freeze dried. Samples were snap frozen at −196 °C using liquid nitrogen and freeze dried for 72 h using a Lablyo mini freeze dryer (Frozen in Time, UK). Freeze drying was performed under high vacuum conditions (4×10^{-4} mbar) with the condenser temperature set at −55 °C. Following this process, the cells and tubes were imaged using a TM3030 table top scanning electron microscope (Hitachi,

Japan). The other proportion of cells and tubes were permeabilised using 0.5% Triton X-100, stained with Phalloidin, CF 488A conjugate (Biotium, United States) and mounted on slides using ProLong™ Gold Antifade Mountant with DAPI (Invitrogen, US). Images were acquired using a DM6000 Fluorescence Microscope (Leica, Germany) and processed using ImageJ software (Java 1.8.0_172).

Results and discussion

Evolution of chemobiotic morphologies

Chemobrionic calcium phosphate structures generated from dibasic sodium phosphate solutions (0.2–1 M) appear as white tube structures that form twisting patterns in the horizontal plane and grow upward through the phosphate solution (Fig. 1a). Tubes were slow to form when calcium hydrogels were layered with phosphate solutions between 0.2–0.3 M, with no tubes observed after 1 h. When the phosphate solution concentration was increased to 0.35 M, tubes were visible after approximately 30 min. After a prolonged induction time, tubes were seen to have formed in phosphate solutions of 0.2–0.4 M (Fig. 1b). This phenomenon of no immediate formation followed by the growth of structures may be a consequence of the relatively low concentration of phosphate present. Although

system dependent, it has been shown that a longer induction time is needed for the formation and subsequent rupture of a colloidal semi-permeable membrane when the anionic reservoir concentration is decreased.[6,13]

Interestingly, at higher concentrations of 1 M, 0.9 M, 0.8 M, and infrequently at 0.7 M, a vast majority of structures form through a jetting regime characterised by tubes forming along continuous jets of buoyant metal-ion solution excreted from the gel/solution interface into the bulk phosphate solution. As described previously,[13] calcium ions at the surface of the gel interact with the phosphate ions in the overlaying anionic reservoir resulting in the formation of a colloidal semi-permeable membrane at the gel/solution interface. Water is then drawn across the gel/solution interface causing the hydrogel to swell. Pressure is then spontaneously relieved by rupturing the colloidal precipitate membrane. This results in the emission of streams of cation rich solution that enter the reservoir of reactant anions, giving rise to the precipitation of abiotic monoliths. Continuous growth of structures persists until a state of thermodynamic equilibrium or reactant ion species depletion. It is possible this type of growth occurs more readily at higher phosphate concentrations due to the diffusion, pH and concentration gradients established by a richer anion environment.[6,7]

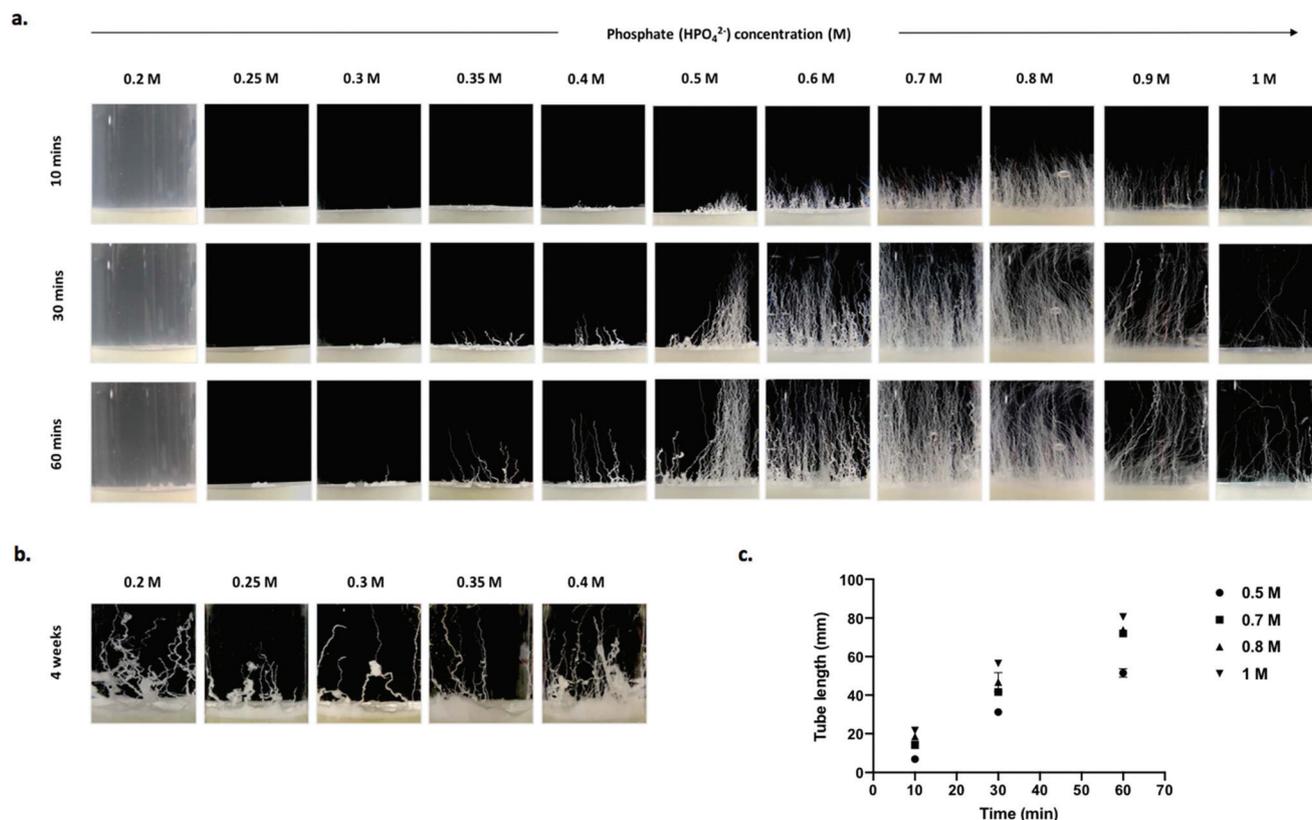Increases in phosphate solution concentration beyond a certain point can hinder and may even prevent structural for-

Fig. 1 Influence of phosphate concentration the growth of chemobrionic scaffolds (field of view is 4.5 cm): (a) generation of structures across a range of phosphate solution concentrations between 0.2–1 M. (b) Formation of structures after a prolonged period of time generated from phosphate solutions between 0.2–0.4 M. (c) Comparative growth curves for calcium phosphate structures generated from 0.5–1 M phosphate solutions.

mation, occurring either through ionic shielding effects or variations in density gradients that are capable of inhibiting advective transport of ions in these systems.[13] Whilst increasing the phosphate concentrations between 0.35–0.8 M proportionally increased both the tube frequency and tube length, at concentrations >0.9 M, the frequency of tubes decreased, while the tube length continued to increase. After 60 min, tubes grown from 1 M phosphate solutions reached 80 mm, while tubes grown from 0.8 M phosphate solution reached 74 mm, although the frequency of tubes grown from 0.8 M phosphate far exceeds that of the 1 M phosphate system (Fig. 1a and c). However, the concentration is proportional to the osmotic pressure which facilitates tube growth. Therefore, our observations are in agreement with the theoretical relationship between osmotic pressure and tube length for a given time frame.[31]

Compositional and microstructural evaluation of selected scaffolds

Autologous tissue has long been considered the "gold standard" for hard tissue regeneration.[28,29] This is tissue that comes from the patient, but may be unsuitable for large defects due to limited quantity that can be harvested. Synthetic grafts, which can be produced in large volumes, are typically based on calcium phosphates that are osteoconductive and sometimes osteoinductive.[30] Advantageously, chemobrionic methods can be used to readily produce structural motifs and frameworks that are analogous to tubular architec-

tures found in bone (*e.g.* Haversian canals, osteons *etc.*). Whilst many examples of chemobrionic structures would not be suitable for implantation due to the toxicological properties of the ionic components employed (see review by Barge *et al.*, for a list of compositional components used to generate chemobrionic structures[1]), architectures generated from calcium and phosphate ions may open up opportunities for biotechnological applications.

To demonstrate proof of concept that materials of this nature may be used as cellular scaffolds, tube structures generated from a 1 M calcium loaded hydrogel layered with 0.8 M dibasic sodium phosphate solution were selected to further examine cell–material interactions. This system exhibits a high degree of reproducibility and is capable of generating a rapid turnover of scaffold frameworks. Tubes confer porosity and micro channels for cellular ingress, which are features that are able to provide an environment for new tissue formation and vascularisation.[31,32] Intricate tubular structures and networks found in mammalian bones and teeth enable nutritional mass transport, facilitating the survival of cells encased deep within these mineralised tissues.[33,34] Tube structures may also provide a framework for fast forming organised vascularised hard tissue.[35]

A decrease in phosphate solution pH was recorded during tube formation, beginning at pH 8.92 for a solution of 0.8 M dibasic sodium diphosphate solution, before gradually shifting to pH 8.78 over the course of approximately 3 h following layering upon calcium loaded hydrogel (Fig. 2a). This is consistent
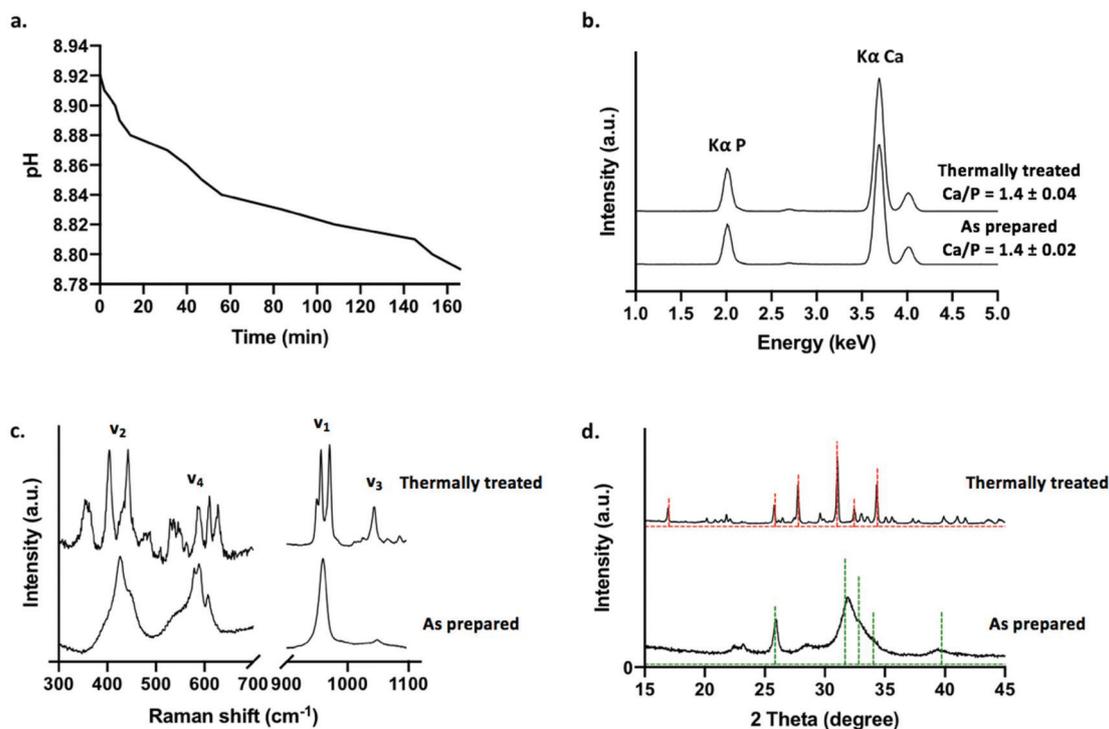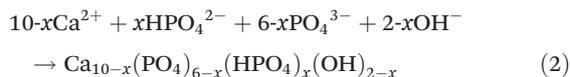

Fig. 2 Generation and characterisation of calcium phosphate tubes: (a) pH evolution of phosphate solution during tube formation. (b) μ-XRF spectra. (c) Raman spectra. (d) XRD patterns (green dashed line = 00-046-0905 reference pattern for CDHA and red dashed line = 00-055-0898 reference pattern for β-TCP).

with the base consuming formation of apatitic mineral from aqueous solutions (eqn (2)).

$$10\text{-}x\text{Ca}^{2+} + x\text{HPO}_4{}^{2-} + 6\text{-}x\text{PO}_4{}^{3-} + 2\text{-}x\text{OH}^-$$
$$\rightarrow \text{Ca}_{10-x}(\text{PO}_4)_{6-x}(\text{HPO}_4)_x(\text{OH})_{2-x} \quad (2)$$

Prior to characterisation, calcium phosphate tubes were washed in water to remove any undesirable soluble phases that may precipitate out of solution whilst drying the structures in air at 50 °C (such as sodium-based salts). A selection of tubes was subjected to a thermal treatment in air at 650 °C for 4 h in order to examine the effects of sintering the ceramic scaffolds on phase evolution. This approach was selected to demonstrate a potential processing route that can be applied to chemobrionic structures in order to achieve alternative compositional formulae of interest. As determined by XRF spectroscopy, structures comprised primarily of calcium and phosphorus (in the form of phosphate) (Fig. 2b). No significant difference was found between the Ca/P ratio of as prepared (Ca/P = 1.4 ± 0.02) and thermally treated tubes (Ca/P = 1.4 ± 0.04) (p = 0.1) (Fig. 2b). Whilst stoichiometric hydroxyapatite (HA, ($\text{Ca}_{10}(\text{PO}_4)_6\text{OH}_2$) has a Ca : P ratio of 1.67, a combination of impurities, ionic vacancies and calcium deficiencies can result in apatitic mineral with a Ca/P ratio as low as 1.3.[36]

Raman spectroscopy was used to identify and differentiate calcium phosphate phases based on vibrational modes arising from $\text{H}_2\text{PO}_4{}^-$, $\text{HPO}_4{}^{2-}$ and $\text{PO}_4{}^{3-}$ groups. The Raman spectrum of as prepared tubes was consistent with that of an apatitic phase akin to that of non-stoichiometric HA ($\text{Ca}_{10-x}(\text{PO}_4)_{6-x}(\text{HPO}_4)_x(\text{OH})_{2-x}$ ($0 \leq x \leq 1$)), typically described as calcium deficient HA (CDHA, $\text{Ca}_9(\text{PO}_4)_5\text{HPO}_4\text{OH}$) (Fig. 2c). A peak at 959 cm^{-1} was the most intense and was associated with a weak shoulder at 875 cm^{-1}. These peaks were assigned to the symmetric stretching mode (ν_1) of $\text{PO}_4{}^{3-}$ and $\text{HPO}_4{}^{2-}$ ions respectively of CDHA. Additional peaks located at 427 cm^{-1} and 447 cm^{-1} were assigned to O–P–O symmetric bending (ν_2), 578 cm^{-1}, 591 cm^{-1} and 608 cm^{-1} were assigned to O–P–O asymmetric bending (ν_4) and 1048 cm^{-1} (ν_3) was assigned to the asymmetric stretching of $\text{PO}_4{}^{3-}$ groups.

For thermally treated scaffolds, Raman peak positions representative of specific phosphate ion vibrational modes were substantially altered (Fig. 2c). Two intense bands at 948 cm^{-1} and 971 cm^{-1} were assigned to symmetric stretching mode (ν_1) of the $\text{PO}_4{}^{3-}$ ion associated with beta tricalcium phosphate (β-TCP, β-$\text{Ca}_3(\text{PO}_4)_2$). The splitting of this vibrational mode is characteristic of the β-TCP phase. This suggested the thermal transformation of CDHA to β-TCP (eqn (3)).[37]

$$\text{Ca}_9(\text{PO}_4)_5\text{HPO}_4\text{OH} \rightarrow 3\beta\text{-}\text{Ca}_3(\text{PO}_4)_2 + \text{H}_2\text{O} \quad (3)$$

A peak present at 956 cm^{-1} may be representative of the symmetric stretching mode (ν_1) of the $\text{PO}_4{}^{3-}$ ion arising from any remaining apatite mineral comprising the thermally treated structures. Substantial downshifting of this peak suggests a change in the chemical structure of the apatite phase relating to molecular arrangement, possibly due to the
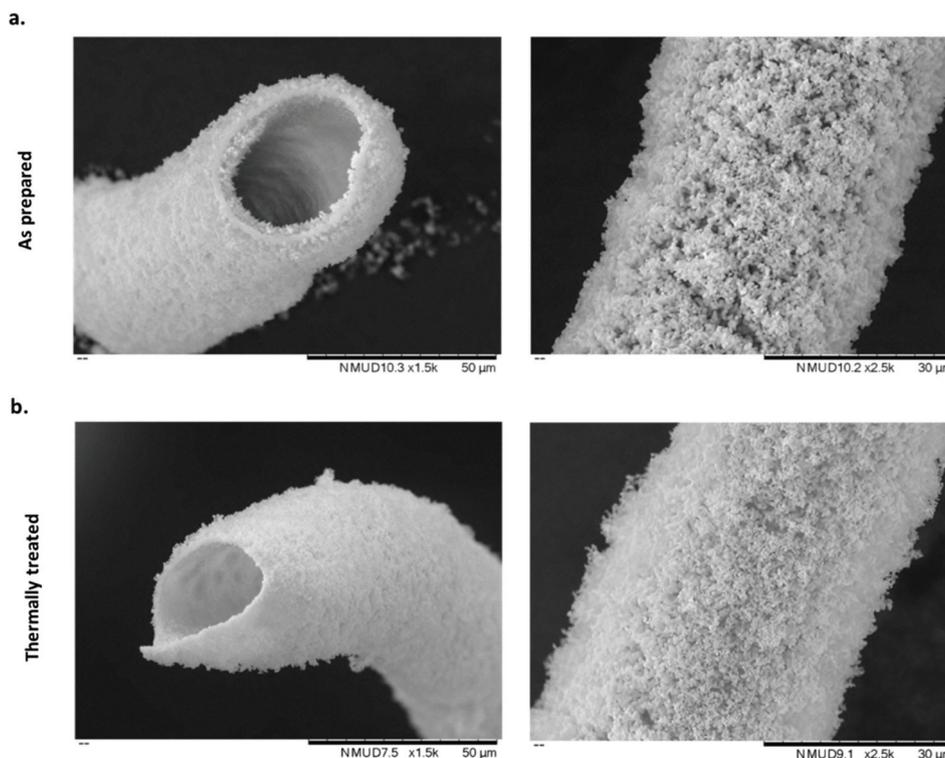

Fig. 3 Microstructural evaluation of calcium phosphate tubes: (a) as prepared calcium phosphate tubes. (b) Thermally treated calcium phosphate tubes.

lengthening of P–O bonds in the changing apatite framework. Peaks between 400–490 cm^{-1} and 530–630 cm^{-1} were assigned to O–P–O symmetric bending (v_2) and O–P–O asymmetric bending (v_4) vibrational modes respectively consistent with β-TCP. A peak at 1044 cm^{-1} was further assigned to the asymmetric stretching mode (v_3) of β-TCP.

XRD was utilised to assess the crystallinity and further confirm the inorganic crystalline composition of as prepared and thermally treated tubes grown using 0.8 M dibasic sodium phosphate solutions (Fig. 1d). Broad peaks were present at 22°, 23°, 26° and 32° 2θ in the diffraction pattern of as prepared tubes suggesting a predominantly amorphous mineral component. Sharper and narrower peaks were present in the diffraction pattern of thermally treated tubes, suggestive of a more mature crystalline phase, with the most predominant peaks present at 26°, 28°, 31° and 34°. In agreement with the calcium phosphate phases identified by Raman spectroscopy, the diffraction patterns of as prepared tubes and thermally treated tubes were matched with diffraction patterns 00-046-0905 for apatitic calcium phosphate, specifically CDHA, and 00-055-0898 for β-TCP respectively, as available from the ICDD database. Both of these phases exhibit a Ca/P of 1.5, which is comparable to the Ca/P ratios determined by XRF spectroscopy for the respective samples. This further confirmed the thermal transformation of non-stoichiometric HA to β-TCP. Additional analysis of the diffraction patterns was used to confirm crystallinity following thermal treatment. As prepared samples were approximately 60–70% crystalline, whereas thermally treated samples were approximately 90% crystalline (determined using eqn (1) by solving for X_c). Moreover, it was estimated that <10% by mass of the thermally treated tubes was composed of remaining apatitic mineral.

SEM was used to analyse the microstructure of calcium phosphate tubes. We previously demonstrated that tubes generated using 0.5 M dibasic ammonium phosphate solutions consist of two microstructurally distinct phases, specifically a porous HA like outer layer and denser dicalcium phosphate dihydrate (DCPD) (also known as the mineral brushite) inner layer.[13] As prepared tubes generated from a 0.8 M dibasic sodium phosphate solution consisted predominantly of a porous outer microstructure (Fig. 3a), not dissimilar to the HA like phase previously reported. Whilst tubes retained a porous
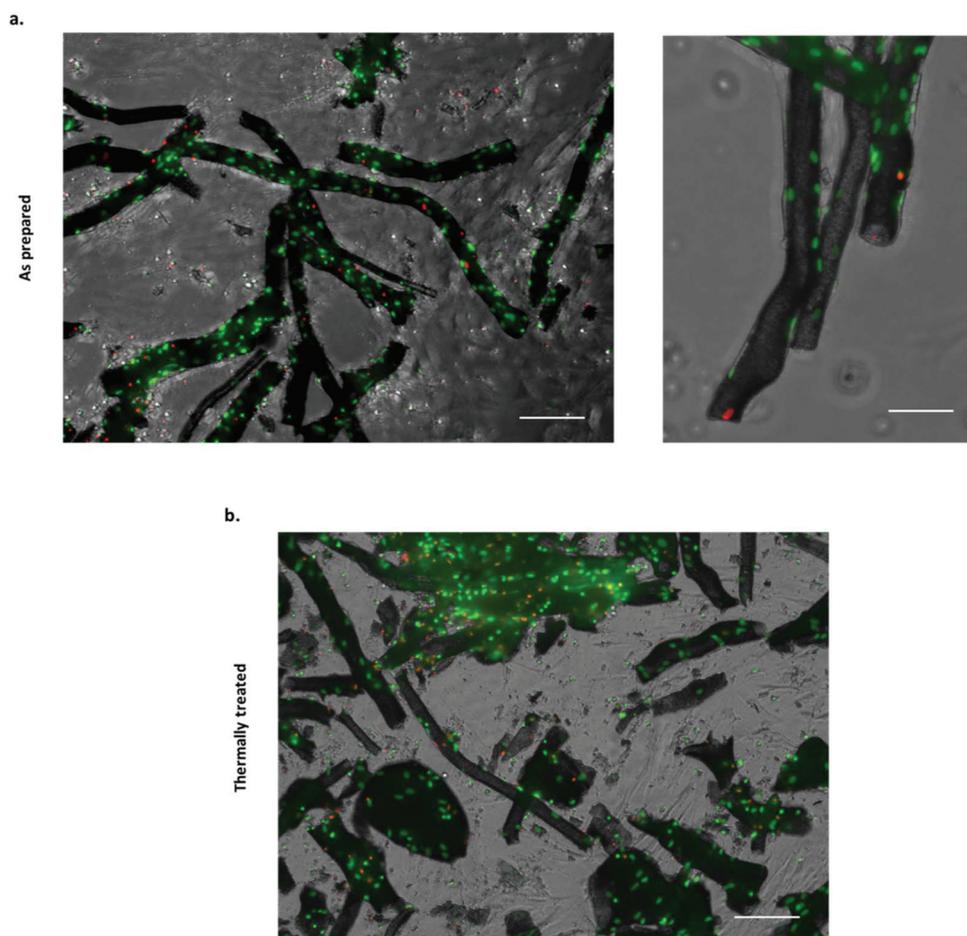

Fig. 4 Viability of BMSCs cultured in direct contact with chemobrionic calcium phosphate tubes (viable cells shown in green (stained with NucBlue® Live) and compromised cells shown in red (stained with NucGreen® Dead)): (a) stained BMSCs associated with thermally as prepared tubes (scale bar = 150 μm for left panel and 75 μm for right panel). (b) Stained BMSCs associated with thermally treated tubes (scale bar = 150 μm).

surface microstructure following thermal treatment, densification of the outer tube wall was evident (Fig. 3b). Helium pycnometry measurements of density (calculated as envelope density) confirmed a significant increase in density from 2.96 ± 0.004 g cm^{-3} to 3.66 ± 0.002 g cm^{-3} ($p = 1.1 \times 10^{-7}$) for as prepared and thermally treated tubes respectively. SEM also showed tubes to be approximately 50 μm in diameter. A broad range of pore diameters between 25–1000 μm has been shown to facilitate osteoblast activity and cellular ingrowth.[38] Pore sizes as small as 50 μm have also been shown to support bone ingrowth *in vivo*.[39]

Cellular interactions with chemobrionic scaffolds

Several approaches have been attempted to study cell–material interactions with chemobrionic scaffolds, including culturing cells in the presence of constructs but not in direct contact,[14] culturing cells in direct contact with constructs[25] and culturing cells entrapped within the precipitated component of the construct.[26] These studies have utilised a variety of cells types, including marine and mammalian cells. For tissue regeneration, specifically the regeneration of human hard tissues, the most relevant cells examined to date are MC3T3 pre-osteoblasts.[14] Whilst these cells were not cultured in direct contact with chemobrionic calcium phosphate scaffolds, the expression of osteogenic markers, including runt-related transcription factor 2 (RUNX2), transcription factor SP7 (SP7), collagen type 1 alpha 1 (COL1A1), and bone gamma-carboxyglutamic acid-containing protein (BGLAP), was significantly upregulated, evidencing the osteoinductive capacity of these materials. In this study, we demonstrate for the first-time direct cell–material interactions between calcium phosphate frameworks of this nature and sheep bone marrow derived mesenchymal stem cells (BMSCs). Stem cells are multipotent progenitors that are capable of differentiating down several specialised cell lineages, including that of bone, cartilage and cardiac cell types, making them highly valuable for applications in tissue engineering.[40,41] Given that cellular adhesion is crucial for cell differentiation, migration and survival, demonstrating the adherence of BMSCs to chemobrionic scaffolds is a pivotal first step toward validating the future developments of materials.[42]

In order to assess cell viability, scaffold BMSC cultures were stained with NucBlue® Live and NucGreen® Dead reagents and imaged using fluorescence microscopy. NucBlue® Live reagent stains mammalian cell nuclei, whilst NucGreen® Dead reagent stains only comprised nuclei. For ease of interpretation, live cells are shown in green and dead cells are shown in red, as opposed to green and blue respectively. Scaffolds demonstrated no adverse cytotoxic effect on BMSCs, the majority of which appeared viable across all samples examined (Fig. 4a and b). Furthermore, viable cells were shown to have adhered to both as prepared and thermally treated tube scaffolds.

Quantitative analysis of the NucBlue® Live and NucGreen® Dead staining images calculated using CellProfiler showed cell viability to be $90.8\% \pm 4.1\%$ for the as prepared scaffolds and $75.8\% \pm 0.1\%$ for the thermally treated scaffolds. It should be noted that the cells were seeded with the tubes in non-adherent plates to maximise the interaction with tubular scaffolds, however, unattached cells would have been subjected to subop-
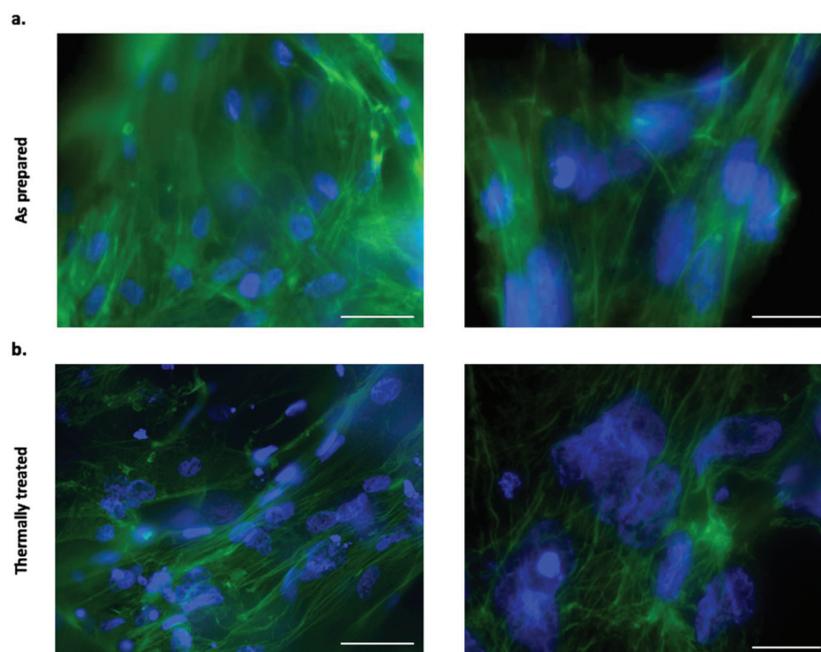

Fig. 5 Cellular actin filament visualisation of BMSCs cultured in direct contact with chemobrionic calcium phosphate tubes showing cell adhesion (F-actin shown in green (stained with CF 488A Phalloidin) and nuclei shown in blue (stained with DAPI)): (a) stained BMSCs associated with as prepared tubes (40× objective, scale bar = 40 μm for left panel and 100× objective, scale bar = 15 μm for right panel). (b) Stained BMSCs associated with thermally treated tubes (40× objective, scale bar = 40 μm for left panel and 100× objective, scale bar = 15 μm for right panel).

timal growth conditions that can lead to cell death. Quantitative analysis was inclusive of both cells attached to the scaffolds and non-adherent cells, suggesting cell adhesion to thermally treated tubes to be less extensive. In cell culture media, the partial fragmentation of the thermally treated scaffolds was observed, likely occurring as a result of additional handling and processing steps. Although damage to the thermally treated scaffolds was not considered extensive being as the majority of tubular structures appeared to remain intact, cell attachment and viability may still have been negatively affected as a consequence.

Filamentous actin was stained with CF 488A Phalloidin to assess the cell adhesion on both as prepared and thermally treated tubes. Fluorescence imaging following staining revealed an extensive level of cellular coverage upon calcium phosphate tubes, which appeared comparable for both as prepared and thermally treated structures (Fig. 5a and b). Samples were further examined using SEM to visualise the morphology of adhered BMSCs upon the chemobrionic frameworks in further detail. In order to preserve and stabilise the cell morphology following removal from the culture environment, we treated the scaffolds firstly with chemical fixative,
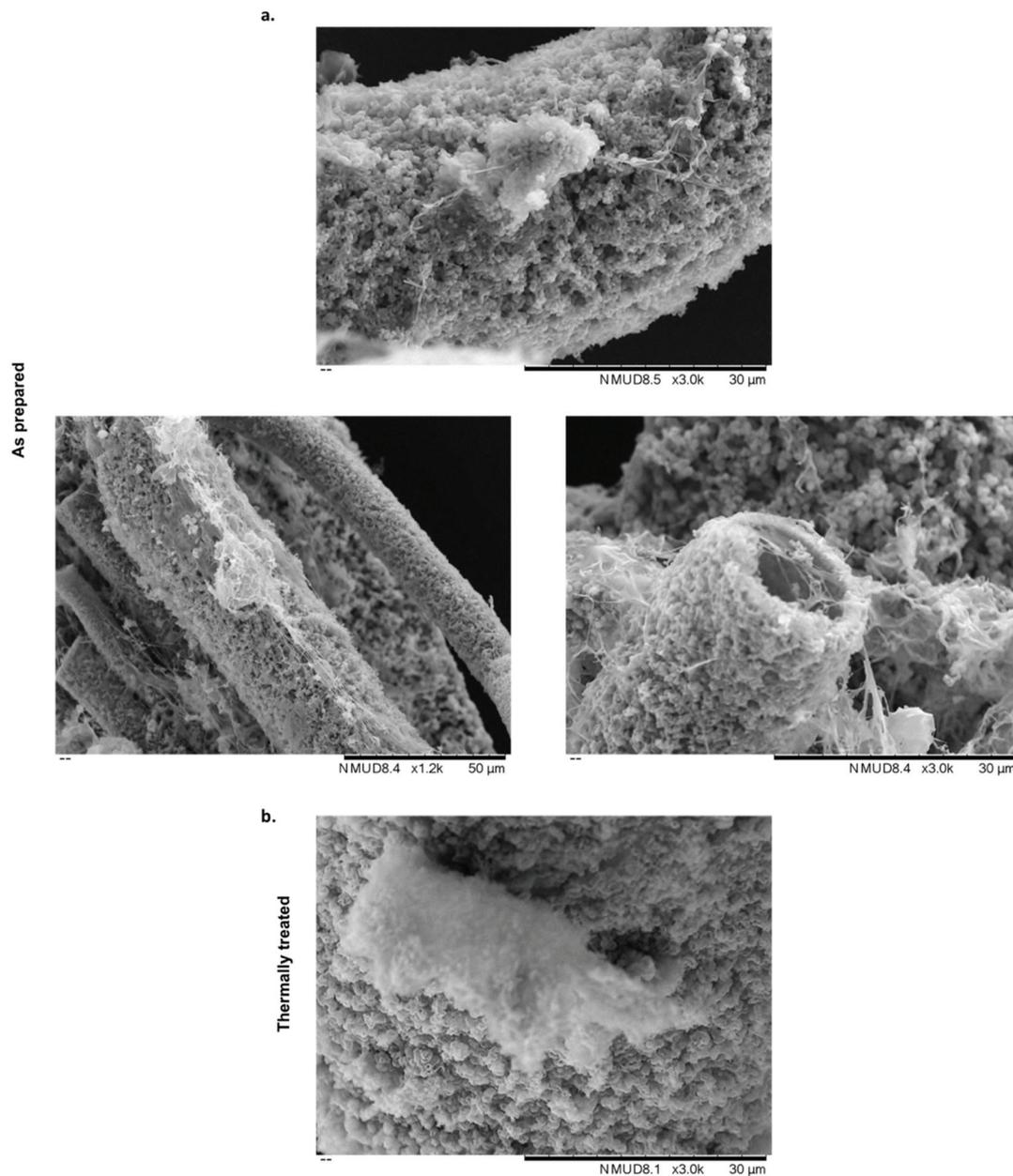

Fig. 6 Morphologies of BMSCs cultured in direct contact with chemobrionic calcium phosphate tubes: (a) BMSCs attached to as prepared calcium phosphate tubes showed an extensive network cell extensions, not only interacting with the outer tube surface but also extending into tube apertures (b) BMSCs attached to thermally treated calcium phosphate tubes showed less extensive spreading and generally appeared more globular.

4% paraformaldehyde solution, followed by placing the scaffolds under vacuum in a freeze-dryer as a means of physical fixation. Although sufficient fixation of cellular components upon porous calcium phosphate substrates may be achieved by freeze-drying alone, scaffolds treated by a combination of chemical and physical fixation methods in succession appear to retain more cells.[43] We observed substantially different cell morphologies dependent on the underlying scaffold within 48 h of cell seeding. BMSCs adhered to as prepared scaffolds showed long multidirectional elongations extending along the outer surface of tubes (Fig. 6a). Cellular elongations were also seen to be interacting with the openings of individual tubular scaffolds, indicating an extensive degree of adaption to the topological features present. Promisingly, the cellular morphologies are comparable to interactions shown between osteogenic scaffolds and human BMSCs.[44] In contrast, BMSCs cells adhered to thermally treated scaffolds displayed less cell spreading, generally presenting a rounded globular morphology with fewer observable elongations (Fig. 6b). Considerable cellular elongation can suggest enhanced interaction with an underlying substrate.[45] It therefore appears that the as prepared tubes comprised of CDHA facilitate a more favourable surface for BMSC adherence. However, F-actin staining (Fig. 5a and b) suggests that BMSCs attached to thermally treated tubes did undergo elongation, possibly comparable to observations made for as prepared scaffolds. Our observed differences in cell adhesion may be influenced by other factors, such as the partial fragmentation of some thermally treated scaffolds (leading to a comparatively lower cell viability).

Various other *in vitro* and *in vivo* studies have assessed cell adhesion and spreading on calcium phosphate substrates. In terms of cytocompatibility, no significant differences have been found between stoichiometric HA and CDHA.[46] Interestingly, increased mesenchymal stem cell cell adhesion and spreading has been shown upon β-TCP compared to HA.[47] Indeed, β-TCP is potentially more osteoinductive compared to HA, whereas HA is potentially more osteoconductive compared to β-TCP.[48] For this reason, scaffolds composed of more than one calcium phosphate phase have been developed in order to combine osteoconductive and osteoinductive properties. It has been reported that material composed of 70% β-TCP and 30% HA promoted elevated expression levels of osteoinductive proteins following implantation in a murine model.[49] Additionally, calcium phosphate scaffolds coated with adhesion proteins prior to cell seeding can improve attachment by four-fold.[50] Furthermore, HA is more stable in the physiological environment in comparison to β-TCP. As such, the ability to fabricate chemobrionic structures composed of apatitic and β-TCP phases may lead to scaffolds that undergo controlled physiologically mediated degradation to promote better conditions for cell interactions and adhesion.[47,48] Our future work will focus on understanding the influence of chemobrionic calcium phosphate tube composition and topology on stimulating cellular biology, adhesion and spreading, as well as promoting osteogenic cell fate. This work also validates the exploration of developing more complex biomaterials for regenerative applications, such as constructs that are formed entirely of or incorporate chemobrionic structures.

Conclusions

Chemobrioinics is a field that describes the formation and self-organisation of abiotic macro-, micro- and nano-architectures by means of diffusion control. To this point, but a few researchers have utilised chemobrionic principles to develop biologically relevant materials for tissue regeneration applications. In this work, chemobrionic approaches are utilised to generate a range of microstructures, including tubular calcium phosphate frameworks composed of CDHA and β-TCP. Viable BMSCs were shown to readily attach to tubes of either composition, with cell morphology indicating that as prepared tubes provide a more favourable surface for interactions. The capacity of these structures to promote osteogenic cell fate is of considerable interest for future studies. Considering the chemical and structural similarity of these materials to human hard tissue, chemobrionic scaffolds could provide ideal candidates for bone regeneration. Mastering control over the generation of these self-assembling architectures may allow for the creation of a new class of chemobrionic biomaterials that can be further modified to enhance tissue growth (*e.g.* surface modification, delivery of growth factors *etc.*).

Conflicts of interest

The authors declare that there are no conflicts of interest to note.

Acknowledgements

References

1 L. M. Barge, S. S. S. Cardoso, J. H. E. Cartwright, G. J. T. Cooper, L. Cronin, A. De Wit, I. J. Doloboff, B. Escribano, R. E. Goldstein, F. Haudin, D. E. H. Jones, A. L. Mackay, J. Maselko, J. J. Pagano, J. Pantaleone,

M. J. Russell, C. I. Sainz-Díaz, O. Steinbock, D. A. Stone, Y. Tanimoto and N. L. Thomas, *Chem. Rev.*, 2015, **115**, 8652–8703.

2 S. S. S. Cardoso and J. H. E. Cartwright, *Proc. R. Soc. A Math. Phys. Eng. Sci.*, 2017, **473**, 20170387.

3 J. H. E. Cartwright, B. Escribano, D. L. González, C. I. Sainz-Díaz and I. Tuval, *Langmuir*, 2013, **29**, 7655–7660.

4 M. B. Short, J. C. Baygents, J. W. Beck, D. A. Stone, R. S. Toomey and R. E. Goldstein, *Phys. Rev. Lett.*, 2005, **94**, 18501.

5 F. Glaab, J. Rieder, J. M. García-Ruiz, W. Kunz and M. Kellermeier, *Phys. Chem. Chem. Phys.*, 2016, **18**, 24850–24858.

6 J. H. E. Cartwright, B. Escribano and C. I. Sainz-Díaz, *Langmuir*, 2011, **27**, 3286–3293.

7 J. H. E. Cartwright, J. M. García-Ruiz, M. L. Novella and F. Otálora, *J. Colloid Interface Sci.*, 2002, **256**, 351–359.

8 F. Glaab, J. Rieder, R. Klein, D. Choquesillo-Lazarte, E. Melero-Garcia, J.-M. García-Ruiz, W. Kunz and M. Kellermeier, *ChemPhysChem*, 2017, **18**, 338–345.

9 J. R. Glauber, in *Furni Novi Philosophici*, Amsterdam, 1646, pp. 186–189.

10 M. Matsuoka, *J. Chem. Educ.*, 2017, **94**, 621–625.

11 S. S. S. Cardoso, J. H. E. Cartwright and C. I. Sainz-díaz, *Icarus*, 2019, **319**, 337–348.

12 C. J. SteenbjergIbsen, B. F. Mikladal, U. BjørnholtJensen and H. Birkedal, *Chem. – Eur. J.*, 2014, **20**, 16112–16120.

13 E. A. B. Hughes, R. L. Williams, S. C. Cox and L. M. Grover, *Langmuir*, 2017, **33**, 2059–2067.

14 E. A. B. Hughes, S. C. Cox, M. E. Cooke, O. G. Davies, R. L. Williams, T. J. Hall and L. M. Grover, *Adv. Healthcare Mater.*, 2018, **7**, 1701166.

15 R. Makki, M. Al-Humiari, S. Dutta and O. Steinbock, *Angew. Chem., Int. Ed.*, 2009, **48**, 8752–8756.

16 B. C. Batista and O. Steinbock, *Chem. Commun.*, 2015, **51**, 12962–12965.

17 S. Wagatsuma, T. Higashi, Y. Sumino and A. Achiwa, *Phys. Rev. E*, 2017, **95**, 52220.

18 B. C. Batista, P. Cruz and O. Steinbock, *Langmuir*, 2014, **30**, 9123–9129.

19 J. J. Pagano, T. Bánsági and O. Steinbock, *J. Phys. Chem. C*, 2007, **111**, 9324–9329.

20 B. T. Burcar, L. M. Barge, D. Trail, E. B. Watson, M. J. Russell and L. B. McGown, *Astrobiology*, 2015, **15**, 509–522.

21 L. M. Barge, Y. Abedian, I. J. Doloboff, J. E. Nuñez, M. J. Russell, R. D. Kidd and I. Kanik, *J. Visualized Exp.*, 2015, 53015.

22 L. M. Barge, Y. Abedian, M. J. Russell, I. J. Doloboff, J. H. E. Cartwright, R. D. Kidd and I. Kanik, *Angew. Chem., Int. Ed.*, 2015, **54**, 8184–8187.

23 C. R. M. Black, V. Goriainov, D. Gibbs, J. Kanczler, R. S. Tare and R. O. C. Oreffo, *Curr. Mol. Biol. Rep.*, 2015, **1**, 132–140.

24 D. Tang, R. S. Tare, L.-Y. Yang, D. F. Williams, K.-L. Ou and R. O. C. Oreffo, *Biomaterials*, 2016, **83**, 363–382.

25 K. Punia, M. Bucaro, A. Mancuso, C. Cuttitta, A. Marsillo, A. Bykov, W. L'Amoreaux and K. S. Raja, *Langmuir*, 2016, **32**, 8748–8758.

26 B. C. Batista, P. Cruz and O. Steinbock, *ChemPhysChem*, 2015, **16**, 2299–2303.

27 H. Markides, J. S. McLaren, N. D. Telling, N. Alom, E. A. Al-Mutheffer, R. O. C. Oreffo, A. Zannettino, B. E. Scammell, L. J. White and A. J. El Haj, *npj Regener. Med.*, 2018, **3**, 9.

28 G. Fernandez de Grado, L. Keller, Y. Idoux-Gillet, Q. Wagner, A.-M. Musset, N. Benkirane-Jessel, F. Bornert and D. Offner, *J. Tissue Eng.*, 2018, **9**, 2041731418776819–2041731418776819.

29 A. Sakkas, F. Wilde, M. Heufelder, K. Winter and A. Schramm, *Int. J. Implant Dent.*, 2017, **3**, 23.

30 J. Jeong, J. H. Kim, J. H. Shim, N. S. Hwang and C. Y. Heo, *Biomater. Res.*, 2019, **23**, 4.

31 L. H. Nguyen, N. Annabi, M. Nikkhah, H. Bae, L. Binan, S. Park, Y. Kang, Y. Yang and A. Khademhosseini, *Tissue Eng., Part B*, 2012, **18**, 363–382.

32 Y. Kang and J. Chang, *Regener. Med.*, 2018, **13**, 705–715.

33 I. S. Maggiano, C. M. Maggiano, J. G. Clement, C. D. L. Thomas, Y. Carter and D. M. L. Cooper, *J. Anat.*, 2016, **228**, 719–732.

34 C. Jud, F. Schaff, I. Zanette, J. Wolf, A. Fehringer and F. Pfeiffer, *Dent. Mater.*, 2016, **32**, 1189–1195.

35 S. Krauss, W. Wagermaier, J. A. Estevez, J. D. Currey and P. Fratzl, *J. Struct. Biol.*, 2011, **175**, 457–464.

36 V. S. Dorozhkin, *Materials*, 2009, **2**, 399–498.

37 A. Siddharthan, S. K. Seshadri and T. S. Sampath Kumar, *Trends Biomater. Artif. Organs*, 2005, **18**, 110–113.

38 K. Kapat, P. Srivas, A. Rameshbabu, P. Maity, S. Jana, J. Dutta, P. Majumdar, D. Chakrabarti and S. Dhara, *ACS Appl. Mater. Interfaces*, 2017, **9**, 39235–39248.

39 A. I. Itälä, H. O. Ylänen, C. Ekholm, K. H. Karlsson and H. T. Aro, *J. Biomed. Mater. Res.*, 2001, **58**, 679–683.

40 B. Heidari, A. Shirazi, M. M. Akhondi, H. Hassanpour, B. Behzadi, M. M. Naderi, A. Sarvari and S. Borjian, *Avicenna J. Med. Biotechnol.*, 2013, **5**, 104–117.

41 A. D. Celiz, J. G. W. Smith, A. K. Patel, A. L. Hook, D. Rajamohan, V. T. George, L. Flatt, M. J. Patel, V. C. Epa, T. Singh, R. Langer, D. G. Anderson, N. D. Allen, D. C. Hay, D. A. Winkler, D. A. Barrett, M. C. Davies, L. E. Young, C. Denning and M. R. Alexander, *Adv. Mater.*, 2015, **27**, 4006–4012.

42 A. A. Khalili and R. M. Ahmad, *Int. J. Mol. Sci.*, 2015, **16**, 18149–18184.

43 J. T. Y. Lee and K. L. Chow, *Scanning*, 2012, **34**, 12–25.

44 C. Matta, C. Szűcs-Somogyi, E. Kon, D. Robinson, T. Neufeld, N. Altschuler, A. Berta, L. Hangody, Z. Veréb and R. Zákány, *Differentiation*, 2019, **107**, 24–34.

45 H. Pan, Y. Xie, Z. Zhang, K. Li, D. Hu, X. Zheng and T. Tang, *RSC Adv.*, 2017, **7**, 8521–8532.

46 H. Guo, J. Su, J. Wei, H. Kong and C. Liu, *Acta Biomater.*, 2009, **5**, 268–278.

47 A. M. C. Barradas, V. Monticone, M. Hulsman, C. Danoux, H. Fernandes, Z. Tahmasebi Birgani, F. Barrère-de Groot, H. Yuan, M. Reinders, P. Habibovic, C. van Blitterswijk and J. de Boer, *Integr. Biol.*, 2013, **5**, 920–931.

48 I. Denry and L. T. Kuhn, *Dent. Mater.*, 2016, **32**, 43–53.

49 J. Wang, Y. Chen, X. Zhu, T. Yuan, Y. Tan, Y. Fan and X. Zhang, *J. Biomed. Mater. Res., Part A*, 2014, **102**, 4234–4243.

50 W. Chen, H. Zhou, M. D. Weir, C. Bao and H. H. K. Xu, *Acta Biomater.*, 2012, **8**, 2297–2306.